Energy & Environmental Science

ROYAL SOCIETY OF CHEMISTRY

PAPER

View Article Online
View Journal

Check for updates

Cite this: DOI: 10.1039/d5ee05739f

Integrated one-step dry process enabling prelithiated thick electrodes without primer coating for high energy density and initial coulombic efficiency

Hyun-Wook Lee, †[a] Woojin Jeong, †[bc] Seongsoo Park,†[d] Ho-Jeong Ji,[a] Ji-Su Woo,[a] Juhyun Lee,[be] Ye-Jin An,[a] Yu-Chan Hwang,[a] Dong-Ha Kim,[a] Hongjun Chang,[d] Minseok Kim,[b] Mikang Jeong,[b] Moonsu Yoon,[b] Dongsoo Lee,[b] Jongsoon Kim,[fg] Zheng-Long Xu,[h] Taeseup Song,[ci] Janghyuk Moon,*[d] Junghyun Choi*[b] and Won-Jin Kwak*[a]

Dry-processed thick electrodes are a key strategy for increasing the energy density of batteries. However, thick dry electrodes, especially anodes, suffer from limited ion mobility, causing non-uniform solid–electrolyte interphase (SEI) formation and high irreversible capacity loss during the initial cycle. Moreover, the adhesive primer layer required during processing increases electrical resistance and necessitates additional wet-processing steps, thereby undermining both performance and process integrity. To address these issues, we propose an underlayer lithium-metal–configured prelithiation strategy for thick electrodes. Here, a lithium metal underlayer simultaneously functions as a primer, compensates for irreversible lithium loss during the initial cycle, and promotes uniform SEI formation through a chemical reaction. Consequently, this strategy enhances the initial coulombic efficiency and cycle stability of high-energy-density silicon–graphite/NCM811 full-cells. By overcoming the limitations of the conventional dry process, a fully dry manufacturing process is enabled and advances the development of next-generation high-energy-density batteries.

Received 27th September 2025,
Accepted 14th January 2026

DOI: 10.1039/d5ee05739f

rsc.li/ees

Open Access Article. Published on 21 January 2026. Downloaded on 2/2/2026 3:14:32 AM.
This article is licensed under a Creative Commons Attribution 3.0 Unported Licence.

Broader context

For long-lasting, high-efficiency, and cost-effective lithium-ion batteries (LIBs), thick electrodes are a promising route to enhance energy density. For the thick electrode manufacturing, the dry-process is particularly attractive as it enables uniform electrode structures without toxic solvents. However, the loss of energy at the initial cycle becomes severe when the electrode thickness is increased, and therefore it is essential to improve the initial coulombic efficiency (ICE). Our study shows one effective approach compensating for the initial loss of energy while fully compatible with the roll-to-roll electrode manufacturing. We demonstrate a prelithiation method utilizing the Li-metal-coated Cu substrate (Li/Cu) ensuring the adhesion between the substrate and composite layer, which is able to substitute for the primer layer. The Li underlayer serves as a reservoir that supplies lithium for solid–electrolyte interphase (SEI) formation and instantly compensates Li loss during the initial cycle reaching 100% of anode ICE and increasing by 20% the ICE of NCM811 full-cell. Moreover, We provide insight in the prelithiation mechanism of Li metal layer implementation through experimental and computational analysis. Synergizing mechanism and application, this work shares understanding-based development of a customized prelithiation method for the dry-process leading to a high-energy-density energy storage system.

[a] School of Energy and Chemical Engineering, UNIST, Ulsan, 44919, Republic of Korea. E-mail: wjkwak@unist.ac.kr
[b] School of Chemical, Biological and Battery Engineering, Gachon University, Seongnam, 13120, Republic of Korea. E-mail: junghchoi@gachon.ac.kr
[c] Department of Energy Engineering, Hanyang University, Seoul 04763, Republic of Korea
[d] Department of Energy Systems Engineering, Chung-Ang University, Seoul, 06974, Republic of Korea. E-mail: jhmoon84@cau.ac.kr
[e] Department of Materials Science and Engineering, Pusan National University, Busan 46241, Republic of Korea
[f] Department of Energy Science, Sungkyunkwan University (SKKU), Suwon 16419, Republic of Korea
[g] SKKU Institute of Energy Science and Technology (SIEST), Sungkyunkwan University, Suwon 16419, Republic of Korea
[h] Department of Industrial and Systems Engineering, The Hong Kong Polytechnic University, Hung Hom, Hong Kong SAR, China
[i] Department of Battery Engineering, Hanyang University, Seoul, 04763, Republic of Korea
† Co-first authors.

Open Access Article. Published on 21 January 2026. Downloaded on 2/2/2026 3:14:32 AM.
This article is licensed under a Creative Commons Attribution 3.0 Unported Licence.

Introduction

As the industrial development of secondary batteries advances, the demand for higher energy density in lithium-ion batteries (LIBs) continues to increase. Strategies to achieve this include modification of active meterials,[1–4] optimization of electrodes,[5–8] and improvements in binders and conductive agents.[9] Among these, thick electrodes are particularly promising, as they reduce the proportion of inactive components, increase the active material content, and thereby enhance both areal capacity and energy density.[10–12] However, thick electrodes fabricated using conventional wet processes often suffer from migration of active and conducting materials during solvent evaporation,[13–15] resulting in non-uniform microstructures and low energy efficiency.[16,17] To address these limitations, the dry process has emerged as a promising alternative. By eliminating organic solvent evaporation—such as that of 1-methyl-2-pyrrolidinone (NMP)—both environmental and economic advantages are afforded, while enabling high energy density.

Despite these benefits, thick film anodes (ThAs) fabricated *via* the dry process face three major challenges: the need for a primer, binder decomposition, and uneven electrode activation. The primer layer, typically wet-coated on the current collector to improve adhesion with the electrode, increases electrical resistance and degrades performance.[18,19] Binder decomposition poses an additional issue: polytetrafluoroethylene (PTFE), the common dry-process binder, has a higher reduction potential than that of polyvinylidene fluoride,[20] thereby lowering the initial coulombic efficiency (ICE). To mitigate PTFE decomposition, fluoroethylene carbonate (FEC) is often added to the electrolyte.[21] However, the ICE of graphite anodes remains only 87% even with FEC, implying that PTFE decomposition is not the sole cause of poor ICE.[22–24] Finally, ThAs suffer from uneven activation owing to limited charge-carrier mobility. As electrode thickness increases, cation mobility becomes restricted, leading to non-uniform current distribution caused by concentration gradients.[25–27] This lack of uniformity results in surface-limited reactions and uneven interphase formation, both of which consume large amounts of Li^+.

To compensate for Li^+ loss, various prelithiation methods have been developed (Fig. 1a). A common method involves Li–arene solutions, where Li^+ forms a complex with arene molecules, enabling electrode lithiation through chemical reaction.[28,29] However, this method requires immersion in solution, making it incompatible with a fully dry process. Direct contact with Li metal (or molten Li) is another approach for prelithiation.[30,31] In this case, Li metal in contact with the active material offsets the loss of Li^+ by solid–electrolyte interphase (SEI) layer formation and improves the anode ICE to nearly 100%.[32] However, direct-contact methods require additional manufacturing steps, such as transfer printing, electrochemical stimulation, or high-temperature treatment.[30,32,33]

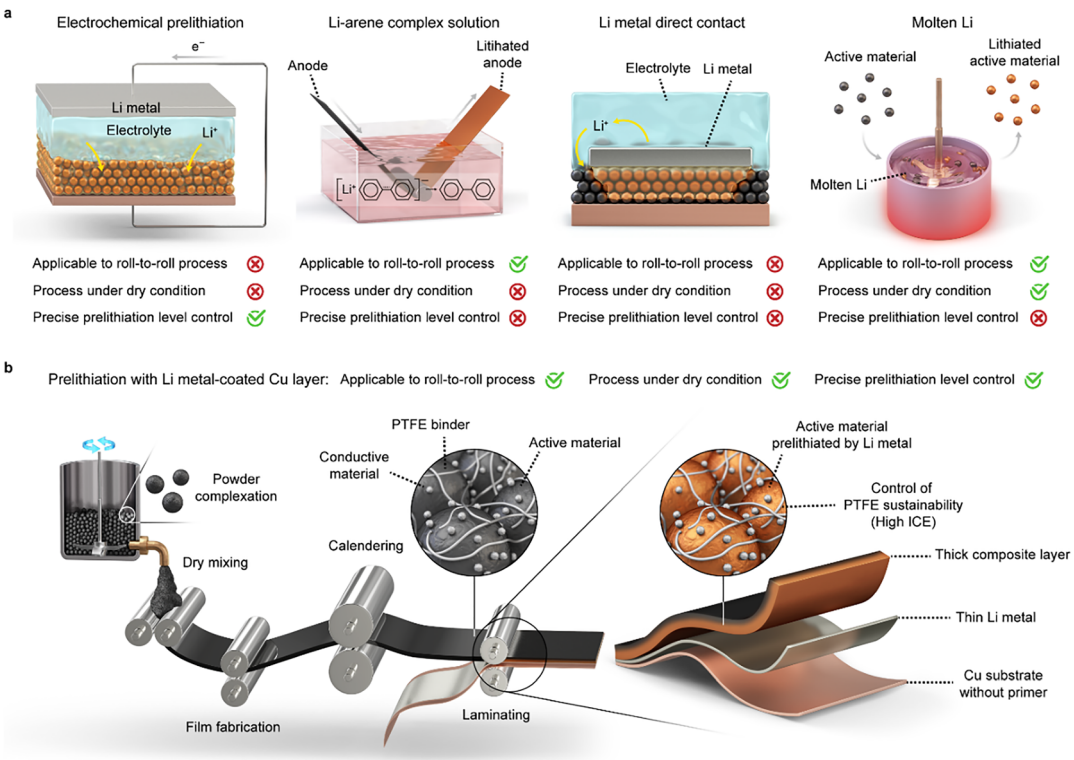


Fig. 1 Comparison of prelithiation methods with factors for practical application. (a) Previously reported prelithiation methods fail to simultaneously meet the key requirements for electrode manufacturing. (b) Proposed one-step prelithiation process using a Li metal-coated Cu layer applied *via* roll-to-roll processing. The Li metal-coated Cu layer ensures layer adhesion and achieves high ICE without the need for a wet-processed primer.

 This journal is © The Royal Society of Chemistry 2026

Open Access Article. Published on 21 January 2026. Downloaded on 2/2/2026 3:14:32 AM.
This article is licensed under a Creative Commons Attribution 3.0 Unported Licence.

That is, prelithiation methods up to now are not suited to the current electrode manufacturing procedure and instead, increase process complexity, thereby limiting compatibility.

To overcome these limitations and enable a fully dry process, we present a primer-free, one-step electrode fabrication and prelithiation strategy using a lithium-metal underlayer (Fig. 1b). This approach uses a lithium-coated Cu (Li/Cu) electrode, allowing simultaneous electrode adhesion and prelithiation without the need for liquids (solvent, electrolyte), or batch-type reactions, and is compatible with the continuous roll-to-roll manufacturing process. The Cu–Li–electrode layer exhibits high adhesion strength, comparable to that between primer-coated Cu (P/Cu) and the electrode, while demonstrating significantly lower resistance. Moreover, the Li metal in Li/Cu serves as a lithium reservoir to compensate for irreversible lithium loss and promotes the formation of a uniform F-rich SEI on the anode, thereby suppressing undesirable electrolyte or Li^+ consumption. Thus, the ICE approaches ~100% in half cells and reaches 93.3% in full cells paired with $LiNi_{0.8}Co_{0.1}Mn_{0.1}O_2$ (NCM811) cathodes, delivering highly stable cycle performance for up to 500 cycles. By unifying dry electrode fabrication and prelithiation into a single step, this conceptual advance improves electrochemical performance and presents a scalable paradigm for practical high-energy-density LIBs.

Results and discussion

Adhesion of dry-processed composite to Li/Cu

Typical dry-processed anodes require a primer to secure adhesion between the electrode composite and current collector.[34] Through roll-to-roll processing, PrL-ThA was successfully fabricated (Fig. 2a and Video S1). Cross-sectional scanning electron microscopy (SEM) confirmed the structural integrity of both ThA and PrL-ThA. ThA consists of three layers–Cu, primer, and silicon/graphite (Si/G). While the Cu and Si/G layers are observable, the primer layer is not, likely owing to its minimal thickness (Fig. S1). Conversely, PrL-ThA shows well-integrated three layers, with a layer of Li metal coated on Cu of ~6.5 μm in thickness, thicker than the primer layer (Fig. 2b). This thickness was precisely optimized to compensate for the first-cycle irreversible capacity loss of the anode, avoiding excess Li plating or dead Li formation, as detailed in Note S1. Notably, the thickness of the composite layer in both electrodes is similar, which implies that the composite layer was controlled precisely, thereby enabling further elucidation of the effect of prelithiation. A folding test was conducted on both ThA and PrL-ThA to compare adhesion levels (Fig. 2c). ThA exhibited no exfoliation of the composite from P/Cu after folding, and similarly, PrL-ThA retained its adhesion even without a primer.

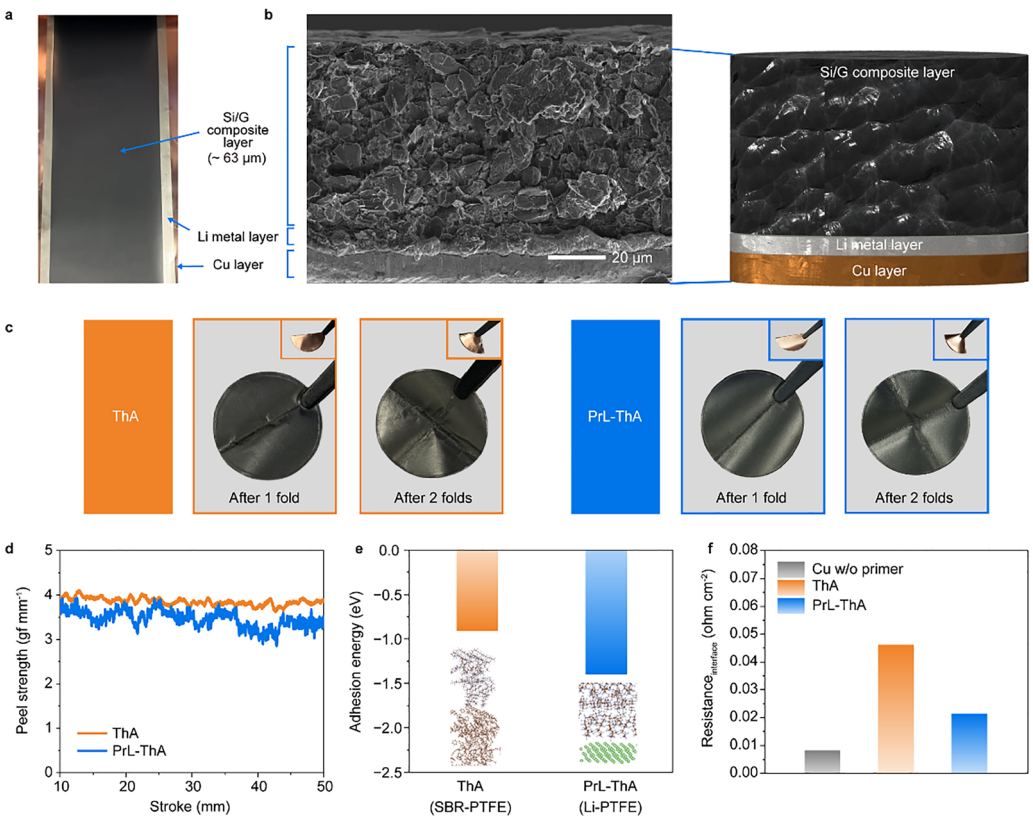


Fig. 2 Comparison of adhesion levels of dry-processed active materials to substrates. (a) Electrodes fabricated *via* roll-to-roll process using PrL-ThA. (b) Cross-sectional SEM image of the PrL-ThA electrode. (c) Folding test of ThA and PrL-ThA using 16 pi disks. (d) Measurement of the force required to peel off the composite layer from substrates. (e) Theoretical calculation of adhesion energy by simulating contact of a primer (orange) or Li metal (blue) with the composite layer. (f) Electrical resistance of electrodes with different substrates, measured under the same pressure, allowing the composite to contact the current collector without a primer.

Open Access Article. Published on 21 January 2026. Downloaded on 2/2/2026 3:14:32 AM. This article is licensed under a Creative Commons Attribution 3.0 Unported Licence.

Fig. 2d shows the peeling strength required to detach the composite from each substrate. Similar values were recorded for both electrodes, confirming that Li provides comparable adhesive strength and can effectively substitute for the primer. Adsorption energy calculations were conducted to compare the affinity between Li and various active materials, as well as current collectors. The results revealed negative adsorption energies for Si, graphite, and Cu, confirming their thermodynamic stability upon interaction with Li (Fig. S2). The adhesion energy between Li and PTFE was compared with that of the conventional styrene butadiene rubber polytetrafluoroethylene (SBR–PTFE) interface (Fig. 2e). The significantly lower adhesion energy of the Li–PTFE pair (−1.39 eV) indicates enhanced interfacial stability compared with that of the conventional SBR-PTFE interface (−0.89 eV). Moreover, the electrical resistance of PrL-ThA is more than twice lower than that of ThA, signifying that the Li metal layer exhibits lower resistance despite being thicker than the primer layer (Fig. 2f). These results highlight the potential advantages of Li/Cu under the electrochemical conditions, including strong adhesion and low resistance.

Uniformity of the SEI layer across the electrode by prelithiation

The thick electrode suffers from limited electrolyte penetration, which contributes to high resistance and non-uniform SEI formation. The effects of lithiation on electrodes were examined *via* time-of-flight secondary ion mass spectrometry (TOF-SIMS) and X-ray photoelectron spectroscopy (XPS). As expected, pristine ThA showed only SiC^- signals on both sides, confirming the absence of lithiation or SEI formation without electrolyte exposure (Fig. S3 and S4). After immersion in electrolyte for 24 h, the front of ThA exhibited LiF_2^- and P^- signals over SiC^- (Fig. 3a and b, left), indicating strong reactions with the electrolyte, whereas the back showed minimal reaction products. XPS profiles of the immersed ThA confirmed these findings (Fig. S5): the front exhibited LiF, whereas the back showed considerably lower levels of LiF and oxygen-containing species, indicating a weaker reaction. These results demonstrate that mere electrolyte contact is insufficient to lithiate the entire thick electrode, resulting in a non-uniform SEI layer. Conversely, PrL-ThA achieved uniform SEI formation even before cycling. Direct contact with Li metal enabled lithiation of active materials through the diffusion of Li^+, even in the absence of electrolyte.[30] X-ray diffraction (XRD) patterns of PrL-ThA exhibited a notable peak shift to lower angles, indicating the formation of a partially lithiated graphite phase (Fig. S6). TOF-SIMS analysis on the back of pristine PrL-ThA revealed dominant $LiSi^-$ signals over those of SiC^- (Fig. S7), confirming Li^+ lithiation. High LiF_2^- contents further indicate that Li^+ reacted with PTFE, contributing to the formation of an inorganic-rich SEI layer.[21,35] XPS spectra provided further insight into early interfacial reactions (Fig. S8). The back of pristine PrL-ThA, where Li metal is in direct contact, exhibited distinct peaks at 685.4 eV corresponding to LiF.[36] These results indicate that Li^+ lowers the electrode potential, lithiating the electrode and reacting with PTFE to form an inorganic SEI layer even in the absence of electrolyte. Following electrolyte application, SEI formation became significantly more pronounced in PrL-ThA. TOF-SIMS profiles of the front of PrL-ThA revealed similar levels of P^- and LiF_2^- to those in ThA (Fig. 3a, right). However, the back of PrL-ThA also exhibited a well-developed inorganic-rich SEI layer, in contrast to the back of ThA (Fig. 3b, right). XPS analysis confirmed the presence of comparable SEI components—including organic carbonates, Li_2CO_3, and LiF—on both sides of PrL-ThA, with characteristic peaks observed at 287, 531.8, and 685.3 eV, respectively (Fig. S9).[37,38] Notably PrL-ThA exhibited enhanced spatial uniformity of SEI species than that of ThA. This suggests that Li^+ diffusion throughout the electrode matrix effectively lowers local potential, promoting electrolyte decomposition even in regions without direct electrolyte contact. Consequently, the spontaneous formation of inorganic-rich SEI layers across the entire electrode depth can be achieved. Specifically, the Li metal at the bottom of the electrode prelithiates the structure and preemptively compensates for Li^+ loss due to binder or electrolyte decomposition during the formation cycle.

Fig. 3c summarizes these experimental results. Without prelithiation, reactions in thick electrodes are limited to the surface, resulting in non-uniform SEI formation and requiring additional Li^+ consumption. Conversely, the Li metal layer in PrL-ThA prelithiates the electrode from the bottom, promoting uniform activation of the entire electrode before cycling. This process enhances SEI uniformity and potentially increases ICE without requiring additional Li^+.

To examine lithiation behavior of active materials under different conditions, FEM simulations were performed for electrolyte-immersed ThA, PrL-ThA, and PrL-ThA with electrolyte (Fig. 3d and e). The presence of Li metal enabled spontaneous lithiation of the electrode through the potential difference between Li and the active materials. However, ThA showed no lithiation, even in the presence of electrolyte. This suggests that LiF detected in the upper region of ThA is attributable to chemical reactions between the electrode and electrolyte alone (Fig. 3a and b, left). Conversely, the Li metal in PrL-ThA acted as a Li reservoir, lithiating the active materials through solid-state diffusion even in the absence of electrolyte. Notably, the SOC variation induced by Li contact resulted in a potential shift in the active materials, which facilitated LiF formation in the bottom region of the electrode (~52%), consistent with experimental results. Furthermore, electrolyte was introduced to PrL-ThA to evaluate electrolyte-mediated lithiation behavior. In this configuration, Li^+ from the Li metal diffused through the electrolyte, lithiating the active materials throughout the electrode thickness. After lithiation, the graphite surfaces located at the top of the electrode exhibited a SOC of at least 6%, indicating that lithiation extended to the uppermost regions of the electrode. To further understand the electrochemical environment, the distributions of both equilibrium potential and electrolyte potential across the electrode were simulated (Fig. S10). Although the equilibrium potential of active materials at the top of the electrode was 0.30 V, higher than the 0.13 V observed at the bottom, the electrolyte potential

 This journal is © The Royal Society of Chemistry 2026

Open Access Article. Published on 21 January 2026. Downloaded on 2/2/2026 3:14:32 AM.
This article is licensed under a Creative Commons Attribution 3.0 Unported Licence.

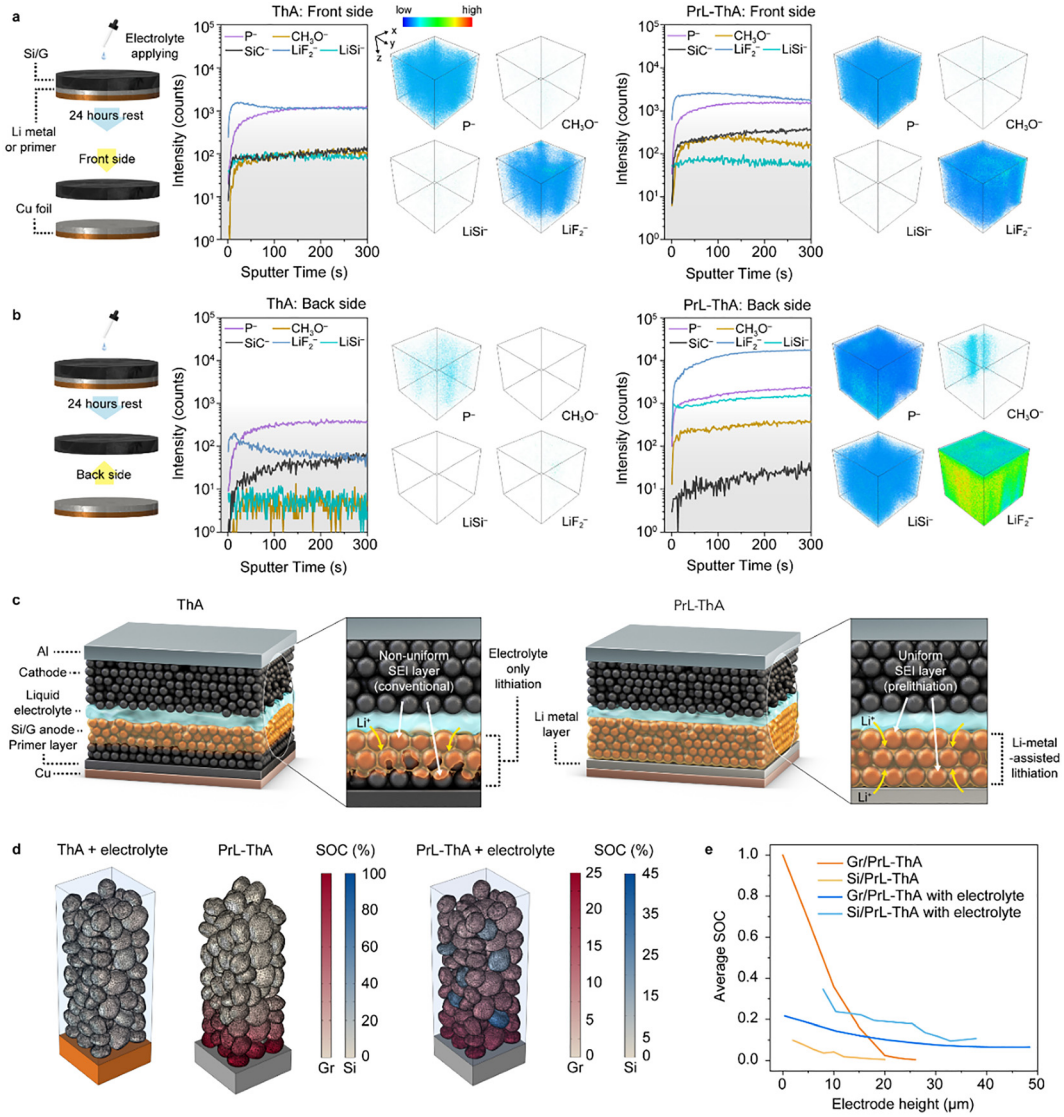


Fig. 3 Lithiation progress and uniformity of electrodes. TOF-SIMS profiles of the (a) front and (b) back of electrodes after electrolyte application, with corresponding 3D reconstruction images. (Left: ThA; Right: PrL-ThA). (c) Schematic illustration of the prelithiation mechanism in a thick electrode. (d) Computational simulation of state-of-charge (SOC) distribution in active material particles under different prelithiation conditions, and (e) SOC distribution of active materials as a function of electrode height.

at the top was substantially lower at −0.27 V compared with −0.035 V at the bottom. This lower electrolyte potential at the top provided sufficient overpotential, thereby enabling lithiation up to the electrode surface. Considering that the open-circuit voltage of graphite at this SOC level (∼0.3 V) is lower than the LiF formation potential range (0.4–0.6 V), LiF formation is expected to occur uniformly across the entire electrode surface. Accordingly, implementing a Li metal layer on the Cu current collector, as proposed in this study, promotes uniform lithiation and LiF formation throughout the electrode, and is anticipated to enhance the electrochemical performance of the cell.

Electrochemical behavior of PrL-ThA and its interface

To investigate the differences between ThA and PrL-ThA, cyclic voltammetry (CV) measurements were conducted. Fig. 4a shows that ThA exhibits a pronounced reduction signal at approximately 0.7 V during the first cycle, corresponding to SEI formation. Conversely, PrL-ThA showed a much weaker reduction signal in the same voltage range, indicating that electrochemically driven SEI formation was largely suppressed. This suggests that in PrL-ThA, the SEI was formed predominantly through chemical reactions initiated by the Li metal layer rather than by electrochemical decomposition of the electrolyte. This suppression of electrolyte decomposition was further verified through half-cell testing (Fig. 4b). ThA released an excess discharge capacity of 68.9 mAh g^{-1} relative to its charge capacity, attributable to electrochemical decomposition of both the electrolyte and PTFE binder. Conversely, PrL-ThA demonstrated an ICE of 100.2%, implying that the prelithiated Li source fully compensated for the Li^+ loss due to side reactions. The SEI properties were further analyzed *via* EIS

Open Access Article. Published on 21 January 2026. Downloaded on 2/2/2026 3:14:32 AM.
This article is licensed under a Creative Commons Attribution 3.0 Unported Licence.

(Fig. 4c, d, Fig. S12 and Table S1). Notably, PrL-ThA exhibited lower impedance than that of ThA, both before and after formation. Specifically, its charge transfer resistance (R_{ct}) was 207.6 ohms before formation, ~40% lower than that of ThA (344.8 ohms). After formation, both R_{ct} and SEI resistance (R_{SEI}) of PrL-ThA remained nearly three times lower than those of ThA, indicating the formation of a low-resistance SEI layer. This favorable property underscores the potential of PrL-ThA for high-rate performance applications. Cycling performance was evaluated in a half-cell configuration. Fig. 4e shows that both ThA and PrL-ThA deliver comparable discharge capacities over 50 cycles, likely owing to the continuous Li supply from the Li metal counter electrode. However, the significantly improved ICE observed for PrL-ThA suggests its potential advantage in full-cell configuration. To further assess the impact of prelithiation on SEI composition after electrochemical operation, XPS depth profiling was performed on both the front and back surfaces of the electrodes post-formation. On the front, the F 1s spectra revealed LiF as the dominant species for both electrodes (Fig. S13a and b). However, ThA exhibited only 33% F content, suggesting a carbon-rich SEI, whereas PrL-ThA displayed 60% F content, indicative of a more inorganic, LiF-enriched interface (Fig. S13c and d). On the back, LiF remained the primary component in both electrodes. Notably, in PrL-ThA, the oxygen content increased progressively with etching depth—a trend absent in ThA (Fig. 4f and g). This observation aligns with TOF-SIMS 3D reconstruction results (Fig. S14), which revealed a uniform distribution of CH_3O^- species across the PrL-ThA back surface. The increasing oxygen signal indicates the formation of a mixed organic–inorganic SEI layer throughout the electrode depth, rather than a purely inorganic one. Supporting this, the atomic ratio of fluorine to oxygen on the back of PrL-ThA was ~1 : 1, compared with 3 : 2 in ThA (Fig. 4h and i), confirming a higher contribution of F-rich inorganic components to the SEI in PrL-ThA. The effectiveness of the F-rich SEI layer on

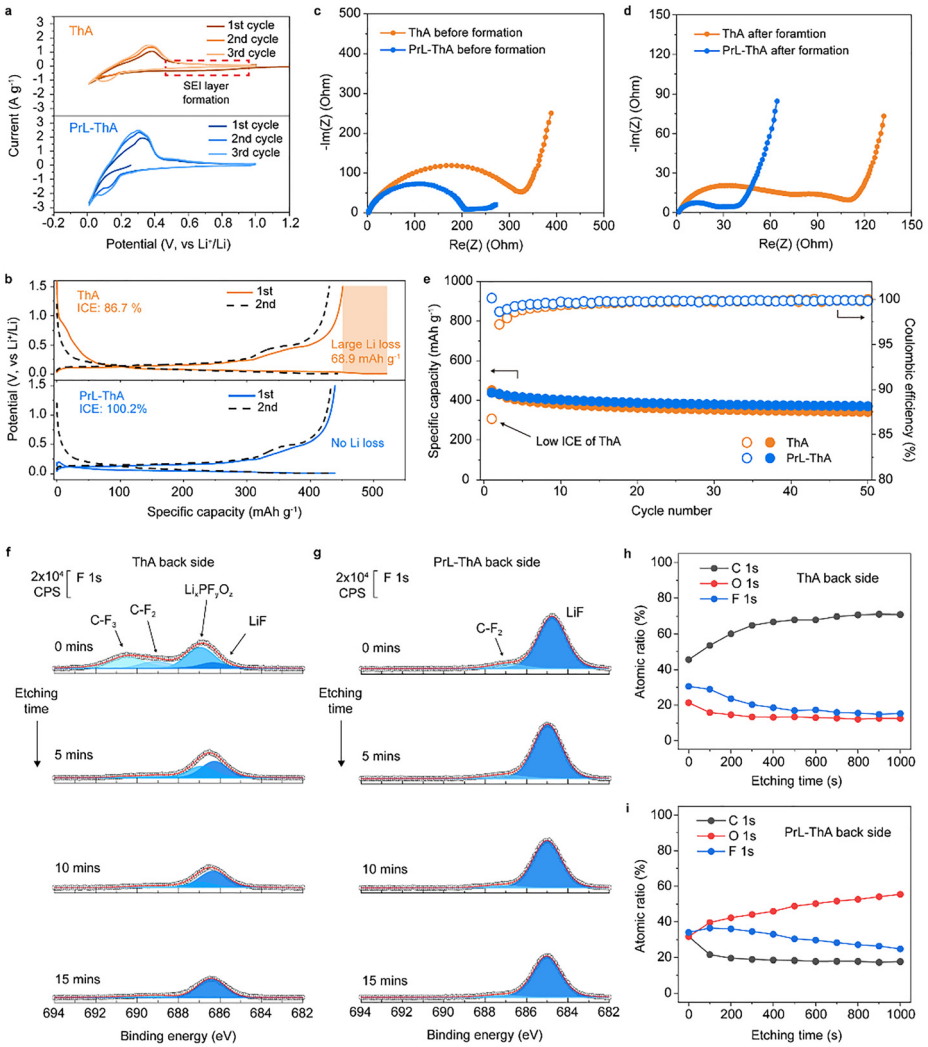


Fig. 4 Effect of prelithiation on electrochemical behavior of the Si/G anode. (a) CV profiles of ThA and PrL-ThA half cells (1.0–0.01 V *vs.* Li^+/Li at 0.1 mV s^{-1}). (b) Charge/discharge profiles (1.5–0.01 V *vs.* Li^+/Li at 0.1C). EIS results (c) before and (d) after formation; equivalent circuit in Fig. S11. (e) Cycle stability. XPS analysis results of electrodes after formation. (f and g) F 1s spectra and (h and i) atomic ratio profiles of the back side of ThA and PrL-ThA.

 This journal is © The Royal Society of Chemistry 2026

Open Access Article. Published on 21 January 2026. Downloaded on 2/2/2026 3:14:32 AM.
This article is licensed under a Creative Commons Attribution 3.0 Unported Licence.

the anode was confirmed by observing Si particles after 20 cycles. The Si particles located on the top of ThA experienced more severe cracking than that on the bottom owing to the concentrated chemical/electrochemical reaction on the top[39–41] (Fig. S15a and b). In addition, the Si particles on PrL-ThA are less damaged, implying that the F-rich SEI layer prevents degradation[42–44] (Fig. S15c and d). Moreover, the Si particles in PrL-ThA exhibit similar intact morphology on the top and bottom, indicating prelithiation induces an even reaction of active materials, increasing the long-term stability of Si particles. These findings highlight that the prelithiation strategy promotes the spontaneous formation of a stable, compositionally balanced SEI layer and even activation during electrochemical operation, contributing to improved performance and Li utilization.

Electrochemical performance of ThA and PrL-ThA in full cells

The full-cell electrochemical performance of ThA and PrL-ThA anodes was evaluated using LFP and NCM811 cathodes. Fig. 5a shows that the PrL-ThA‖LFP full cell demonstrated a significantly higher ICE of 96.6% with an areal capacity of 5.1 mAh cm^{-2}, compared with that of the ThA‖LFP full cell, which had an ICE of 72.1% and a capacity of 3.46 mAh cm^{-2}. This corresponds to improvements of 1.64 mAh cm^{-2} in areal capacity and 24.5% in ICE, underscoring the effectiveness of the prelithiation strategy in compensating for initial Li^+ losses. We note that the physical properties of the electrodes were controlled precisely, and therefore, the difference in the initial discharge capacity of the full-cell with ThA and PrL-ThA is due solely to the prelithiation (Table S2 and Fig. S16). After 197 cycles, the PrL-ThA-based cell displayed a capacity retention of

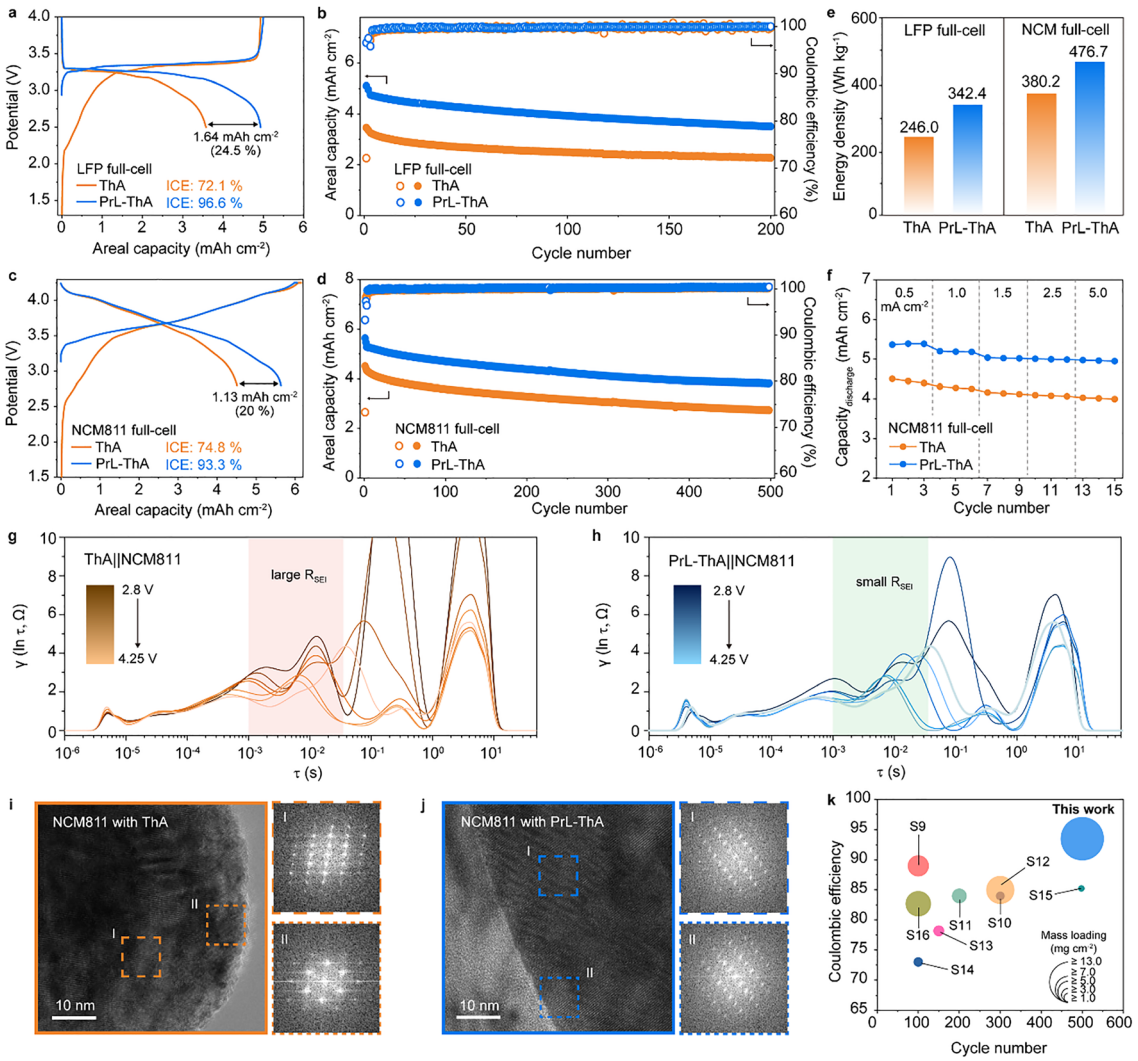


Fig. 5 Electrochemical performance of ThA and PrL-ThA in full-cells. (a) Voltage profiles of the LFP full-cells. (b) Galvanostatic cycling performance of LFP cells over 200 cycles. (c) Voltage profiles of NCM full-cells. (d) Galvanostatic cycling performance of NCM cells over 500 cycles. (e) Comparison of the energy densities of the NCM and LFP cells. (f) Rate capability of the NCM full-cells from 0.5 to 5 mA cm^{-2}. *In situ* DRT spectra of NCM811 full-cells with (g) ThA and (h) PrL-ThA during the first formation charge from 2.8 to 4.25 V with incremental cut-off steps of ΔV = 0.21 V. TEM images and FFT patterns of the NCM811 cathode after cycling with (i) ThA and (j) PrL-ThA. (k) Comparison with recent reports highlighting the practical potential of the PrL-ThA full-cell with its high ICE, cyclability, and mass loading level.

Open Access Article. Published on 21 January 2026. Downloaded on 2/2/2026 3:14:32 AM. This article is licensed under a Creative Commons Attribution 3.0 Unported Licence.

74.1%, outperforming the ThA-based cell, which retained only 68.2% (Fig. 5b). In NCM811-based full cells (Fig. 5c and d), PrL-ThA‖NCM similarly outperformed ThA‖NCM, achieving an areal capacity of 5.63 mAh cm^{-2} and an ICE of 93.3%, which translated to 1.13 mAh cm^{-2} and 20% improvements, respectively. The improvement shown by prelithiation is similar to or even higher than the theoretically calculated value (Fig. S17 and S18), owing to the synergistic effect of the structural stability of the active materials, which will be further demonstrated. These results highlight that prelithiation significantly compensates for lithium consumption associated with SEI formation and PTFE decomposition, thereby enhancing the reversibility of the anode in full-cell configurations. Fig. 5e demonstrates that the first-cycle energy densities of PrL-ThA full cells improved by 25.4% in NCM and 39.2% in LFP cells. These improvements were sustained over extended cycling, as confirmed by Fig. S19 and S20. Rate testing validated the superior behavior of PrL-ThA (Fig. 5f). Across a wide range of current densities (0.5–5 mA cm^{-2}), the PrL-ThA cell maintained higher discharge capacities, indicating minimal active lithium loss and robust interfacial stability. The evolution of the SEI layer on the anode was confirmed by XPS as a function of state of charge in a full-cell configuration. Similar to that demonstrated previously, the back of ThA has severe incomplete decomposition of electrolyte (Fig. S21a). Further, PrL-ThA exhibits a uniform LiF-rich SEI layer across the electrode, consistent with the results from the half-cell condition (Fig. S21b). The interfacial behavior was further elucidated by *in situ* EIS combined with a distribution of relaxation times (DRT) analysis (Fig. 5g, h and Fig. S22). In the ThA‖NCM811 full cell, the interfacial resistance components, including the R_{SEI} originating from both the cathode and anode surfaces, exhibited noticeable fluctuations during the charging process, indicating that the interphase was not fully stabilized and responded sensitively to changes in the applied voltage. Conversely, the PrL-ThA‖NCM811 full cell maintained consistently low and stable interfacial resistance values across all charging steps, suggesting that the Li/Cu-based prelithiation process had already established a robust LiF-rich interphase that effectively mitigates further SEI thickening and electrolyte-induced parasitic reactions. The structural stability of the NCM811 cathode after long-term cycling was investigated using transmission electron microscopy (TEM) and corresponding fast Fourier transform (FFT) pattern analysis (Fig. 5i and j). The NCM811 cathode paired with ThA showed surface roughening and partial transformation to a rock-salt phase, accompanied by disordered FFT patterns—hallmarks of significant structural degradation. Conversely, the NCM811 particles cycled with PrL-ThA retained a well-defined layered structure and consistent FFT patterns, indicating that PrL-ThA protects the anode and suppresses cathode degradation during extended cycling. Finally, a comparative analysis with state-of-the-art full-cell reports (Fig. 5k and Table S3) demonstrates that the PrL-ThA full cell achieves an exceptional balance of high areal capacity, elevated energy density, and practical mass loading, emphasizing its potential for next-generation high-energy-density LIBs.

Conclusions

We report a simple one-step dry strategy in which a Li/Cu foil serves as a lithium source to effectively prelithiate Si/G thick anodes, eliminating the need for primers or wet treatment. The resulting PrL-ThA electrodes suppress initial Li^+ loss, maintain adhesion comparable with that of conventional thick anodes, and exhibit lower resistance owing to the absence of insulating primers. Solid-state diffusion from the Li/Cu foil enables uniform lithiation and SEI formation, yielding ~100% ICE in half cells and 93.3% in full cells with NCM811, with an energy density of 476.7 Wh kg^{-1}. Moreover, the reduced Li^+ demand alleviates structural degradation of the NCM811 cathode, while the fully dry and roll-to-roll-compatible process eliminates the complexity of electrodeposition and transfer-printing-based methods, positioning this approach as a scalable and practical pathway for next-generation high-energy-density lithium-ion batteries.

Author contributions

H.-W. L., W. J., and S. P. contributed to conceptualization, investigation, visualization, writing the original draft, manuscript reviewing, and editing. H.-J. J., J.-S. W., and Y.-J. A. contributed to the investigation and review of the manuscript. S. P., H. C. performed the computational simulations. J. L., M. K., M. J., M. Y., D. L., J. K., Z.-L. X., and T. S. contributed to formal analysis and review of the manuscript. J. M., J. C., and W.-J. K. contributed to conceptualization, funding acquisition, and manuscript review and editing.

Conflicts of interest

A patent related to the application in anode preparation: Kwak, W.-J.; Woo, J.-S.; Choi, J.; Lee, J. ''Method of preparing a dry anode for lithium secondary battery and dry anode for lithium secondary battery'' Korean Patent Application No. 10-2024-0058602, Filing Date: 05/22/2024. The remaining authors declare no competing interests.

Data availability

The data supporting this article have been included as part of the supplementary information (SI). Supplementary information is available. See DOI: https://doi.org/10.1039/d5ee05739f.

Acknowledgements

W.-J. K. acknowledges support from the Technology Innovation Program (20024252, Development of highly impregnative liquid electrolyte for high-performance lithium iron phosphate battery with thick electrode), funded by the Ministry of Trade, Industry & Energy (MOTIE, Korea). J. C. acknowledges support from the National R&D Program through the National Research Foundation of Korea (NRF), funded by the Ministry of Science and ICT (No. RS-2024-00408156). This study contains the

 This journal is © The Royal Society of Chemistry 2026

Open Access Article. Published on 21 January 2026. Downloaded on 2/2/2026 3:14:32 AM. This article is licensed under a Creative Commons Attribution 3.0 Unported Licence.

results obtained by using the equipment from UNIST Central Research Facilities (UCRF).

Notes and references

1 G. Liang, V. K. Peterson, Z. Wu, S. Zhang, J. Hao, C. Lu, C. Chuang, J. Lee, J. Liu, G. Leniec, S. M. Kaczmarek, A. M. D'Angelo, B. Johannessen, L. Thomsen, W. K. Pang and Z. Guo, *Adv. Mater.*, 2021, 101413.
2 H. Jia, X. Li, J. Song, X. Zhang, L. Luo, Y. He, B. Li, Y. Cai, S. Hu, X. Xiao, C. Wang, K. M. Rosso, R. Yi, R. Patel and J.-G. Zhang, *Nat. Commun.*, 2020, **11**, 1474.
3 W. Zhao, L. Zou, H. Jia, J. Zheng, D. Wang, J. Song, C. Hong, R. Liu, W. Xu, Y. Yang, J. Xiao, C. Wang and J.-G. Zhang, *ACS Appl. Energy Mater.*, 2020, **3**, 3369–3377.
4 N. Kim, Y. Kim, J. Sung and J. Cho, *Nat. Energy*, 2023, **8**, 921–933.
5 N. Ogihara, S. Kawauchi, C. Okuda, Y. Itou, Y. Takeuchi and Y. Ukyo, *J. Electrochem. Soc.*, 2012, **159**, A1034–A1039.
6 Z. Ju, Y. Zhu, X. Zhang, D. M. Lutz, Z. Fang, K. J. Takeuchi, E. S. Takeuchi, A. C. Marschilok and G. Yu, *Chem. Mater.*, 2020, **32**, 1684–1692.
7 S. Müller, P. Pietsch, B.-E. Brandt, P. Baade, V. De Andrade, F. De Carlo and V. Wood, *Nat. Commun.*, 2018, **9**, 2340.
8 X. Lu, S. R. Daemi, A. Bertei, M. D. R. Kok, K. B. O'Regan, L. Rasha, J. Park, G. Hinds, E. Kendrick, D. J. L. Brett and P. R. Shearing, *Joule*, 2020, **4**, 2746–2768.
9 H. Oh, G.-S. Kim, J. Bang, S. Kim and K.-M. Jeong, *Energy Environ. Sci.*, 2025, **18**, 645–658.
10 Y. Li, S. Song, H. Kim, K. Nomoto, H. Kim, X. Sun, S. Hori, K. Suzuki, N. Matsui, M. Hirayama, T. Mizoguchi, T. Saito, T. Kamiyama and R. Kanno, *Science*, 2023, **381**, 50–53.
11 M. S. Kang, I. Heo, S. Kim, J. Yang, J. Kim, S.-J. Min, J. Chae and W. C. Yoo, *Energy Storage Mater.*, 2022, **50**, 234–242.
12 Z. Su, W. Ren, H. Guo, X. Peng, X. Chen and C. Zhao, *Adv. Funct. Mater.*, 2020, 2005477.
13 J. Kumberg, M. Müller, R. Diehm, S. Spiegel, C. Wachsmann, W. Bauer, P. Scharfer and W. Schabel, *Energy Technol.*, 2019, **7**, 1900722.
14 J. Klemens, L. Schneider, E. C. Herbst, N. Bohn, M. Müller, W. Bauer, P. Scharfer and W. Schabel, *Energy Technol.*, 2021, **10**, 2100985.
15 H. Wang, Y. Chen, Y. Song and D. Xiong, *J. Energy Storage*, 2025, **118**, 116288.
16 Y. Guo, X. Li, H. Guo, Q. Qin, Z. Wang, J. Wang and G. Yan, *Energy Storage Mater.*, 2022, **51**, 476–485.
17 K. Ko, K. Kim, Y. Kim, S. Han, J. Park, H. Park, J. Yang, B. Kim, J. Park and K. Kang, *Small*, 2024, **21**, 2410795.
18 N.-Y. Kim, J.-H. Kim, H. Koo, J. Oh, J.-H. Pang, K.-D. Kang, S.-S. Chae, J. Lim, K. W. Nam and S.-Y. Lee, *ACS Energy Lett.*, 2024, **9**, 5688–5703.
19 D. Burger, N. Keim, J. Shabbir, Y. Gao, M. Müller, W. Bauer, A. Hoffmann, P. Scharfer and W. Schabel, *Energy Technol.*, 2024, **13**, 2401668.
20 Z. Wei, D. Kong, L. Quan, J. He, J. Liu, Z. Tang, S. Chen, Q. Cai, R. Zhang, H. Liu, K. Xu, L. Xing and W. Li, *Joule*, 2024, **8**, 1350–1363.
21 S. Han, E.-H. Noh, S. Chae, K. Kwon, J. Lee, J.-S. Woo, S. Park, J. W. Lee, P. J. Kim, T. Song, W.-J. Kwak and J. Choi, *J. Energy Storage*, 2024, **96**, 112693.
22 T. Lee, J. An, W. J. Chung, H. Kim, Y. Cho, H. Song, H. Lee, J. H. Kang and J. W. Choi, *ACS Appl. Mater. Interfaces*, 2024, **16**, 8930–8938.
23 G. Li, *Solid State Ion*, 1996, **90**, 221–225.
24 R. Tao, B. Steinhoff, X.-G. Sun, K. Sardo, B. Skelly, H. M. Meyer, C. Sawicki, G. Polizos, X. Lyu, Z. Du, J. Yang, K. Hong and J. Li, *Chem. Eng. J.*, 2023, **471**, 144300.
25 T. Danner, M. Singh, S. Hein, J. Kaiser, H. Hahn and A. Latz, *J. Power Sources*, 2016, **334**, 191–201.
26 K.-Y. Park, J.-W. Park, W. M. Seong, K. Yoon, T.-H. Hwang, K.-H. Ko, J.-H. Han, Y. Jaedong and K. Kang, *J. Power Sources*, 2020, **468**, 228369.
27 L. S. Kremer, T. Danner, S. Hein, A. Hoffmann, B. Prifling, V. Schmidt, A. Latz and M. Wohlfahrt-Mehrens, *Batteries Supercaps*, 2020, **3**, 1172–1182.
28 J. Choi, H. Jeong, J. Jang, A.-R. Jeon, I. Kang, M. Kwon, J. Hong and M. Lee, *J. Am. Chem. Soc.*, 2021, **143**, 9169–9176.
29 Y. Shen, X. Shen, M. Yang, J. Qian, Y. Cao, H. Yang, Y. Luo and X. Ai, *Adv. Funct. Mater.*, 2021, **31**, 2101181.
30 J. Lee, D. Jin, J. Y. Kim, Y. Roh, H. Lee, S. H. Kang, J. Choi, T. Jo, Y. Lee and Y. M. Lee, *Adv. Energy Mater.*, 2023, **13**, 2300172.
31 P. Bärmann, M. Mohrhardt, J. E. Frerichs, M. Helling, A. Kolesnikov, S. Klabunde, S. Nowak, M. R. Hansen, M. Winter and T. Placke, *Adv. Energy Mater.*, 2021, **11**, 2100925.
32 C. Yang, H. Ma, R. Yuan, K. Wang, K. Liu, Y. Long, F. Xu, L. Li, H. Zhang, Y. Zhang, X. Li and H. Wu, *Nat. Energy*, 2023, **8**, 703–713.
33 H. Dong, T. Yang, C. Liu, D. Luo, N. Liu, Y. Gao, Z. Shi, Y. Zhang and Z. Chen, *Energy Storage Mater.*, 2025, **75**, 104072.
34 W. Jin, G. Song, J. Yoo, S. Jung, T. Kim and J. Kim, *ChemElectroChem*, 2024, **11**, e202400288.
35 S. Shiraishi, T. Kobayashi and A. Oya, *Chem. Lett.*, 2005, **34**, 1678–1679.
36 A. N. Mansour, D. G. Kwabi, R. A. Quinlan, Y.-C. Lu and Y. Shao-Horn, *J. Electrochem. Soc.*, 2016, **163**, A2911–A2918.
37 J. Heine, P. Hilbig, X. Qi, P. Niehoff, M. Winter and P. Bieker, *J. Electrochem. Soc.*, 2015, **162**, A1094–A1101.
38 A. Augustsson, M. Herstedt, J.-H. Guo, K. Edström, G. V. Zhuang, P. N. Ross Jr., J.-E. Rubensson and J. Nordgren, *Phys. Chem. Chem. Phys.*, 2004, **6**, 4185–4189.
39 X. Lu, M. Lagnoni, A. Bertei, S. Das, R. E. Owen, Q. Li, K. O'Regan, A. Wade, D. P. Finegan, E. Kendrick, M. Z. Bazant, D. J. L. Brett and P. R. Shearing, *Nat. Commun.*, 2023, **14**, 5127.
40 L. Lin, F. Dong, J. Tao, Y. Tu, H. Lin, Y. Lin and Z. Huang, *Phys. Rev. Appl.*, 2025, **24**, 014057.

41 Z. Li, L. Yin, G. S. Mattei, M. R. Cosby, B.-S. Lee, Z. Wu, S.-M. Bak, K. W. Chapman, X.-Q. Yang, P. Liu and P. G. Khalifah, *Chem. Mater.*, 2020, **32**, 6358–6364.
42 Z. Cao, X. Zheng, Q. Qu, Y. Huang and H. Zheng, *Adv. Mater.*, 2021, **33**, 2103178.
43 K. Schroder, J. Alvarado, T. A. Yersak, J. Li, N. Dudney, L. J. Webb, Y. S. Meng and K. J. Stevenson, *Chem. Mater.*, 2015, **27**, 5531–5542.
44 L. Quan, Q. Su, H. Lei, W. Zhang, Y. Deng, J. He, Y. Lu, Z. Li, H. Liu, L. Xing and W. Li, *Natl. Sci. Rev.*, 2025, **12**, nwaf084.

Open Access Article. Published on 21 January 2026. Downloaded on 2/2/2026 3:14:32 AM.
This article is licensed under a Creative Commons Attribution 3.0 Unported Licence.

This journal is © The Royal Society of Chemistry 2026